Temperature mapping in bread dough using SE and GE two-point MRI methods: experimental and theoretical estimation of uncertainty

T. Lucas, Maja Musse, Melanie Bornert, A. Davenel, S. Quellec

Elsevier Editorial System(tm) for Magnetic Resonance Imaging
Manuscript Draft

Manuscript Number: MRI-D-10-00237R2

Title: Temperature mapping in bread dough using SE and GE two-point MRI methods: experimental and theoretical estimation of uncertainty

Article Type: Original Contribution

Keywords: MRI; temperature mapping; T1; dough; bread; uncertainty; food

Corresponding Author: Dr Maja Musse, Ph. D.

Corresponding Author's Institution: Cemagref

First Author: Tiphaine Lucas, Ph.D.

Order of Authors: Tiphaine Lucas, Ph.D.; Maja Musse, Ph.D.; Mélanie Bornert; Armel Davenel, Ph.D.; Stéphane Quellec

Abstract

2D-SE, 2D-GE and 3D-GE two-point T_1-weighted MRI methods were evaluated in this study in order to maximise the accuracy of temperature mapping of bread dough during thermal processing. Uncertainties were propagated throughout each protocol of measurement, and comparisons demonstrated that all the methods with comparable acquisition times minimised the temperature uncertainty to similar extent. The experimental uncertainties obtained with low field MRI were also compared to the theoretical estimations. Some discrepancies were reported between experimental and theoretical values of uncertainties of temperature; however, experimental and theoretical trends with varying parameters agreed to a large extent for both SE and GE methods. The 2D-SE method was chosen for further applications on pre-fermented dough because of its lower sensitivity to susceptibility differences in porous media. It was applied for temperature mapping in pre-fermented dough during chilling prior to freezing and compared locally to optical fiber measurements.

Key words: MRI; temperature mapping; T_1; dough; bread; uncertainty; food; NMR

1 Introduction

Chilling and freezing of dough before proving (unfermented frozen doughs) or just after partial proving (prefermented frozen doughs) are widely used in industrial bakeries to facilitate bread production and baking in retail outlets [1-2]. Such intermediary stages result in spatial and temporal temperature gradients spread over the whole dough. These in turn affect the bubble inflation and the alveolar structure of dough since thermal dilatation, yeast activity and dough rheology which govern bubble inflation together depend directly on temperature.

As invasive measurements may provoke dough collapse, the characterization of the bubble inflation process has long been reduced to a small number of overall volumetric parameters (total dough volume, CO_2 volume released). More recently it has benefited from advances in imaging techniques (e.g. X-ray tomography [3], confocal microscopy [4] and Magnetic Resonance Imaging (MRI)) [5-9]. Many of these previous MRI studies provided quantitative analysis of only large-sized bubbles which can be segmented. Takano *et al.* [7] related the intensity of the MRI signal to the proportion of CO_2 without any form of demonstration. The relationship between MRI grey level and porosity during dough proving (fermentation) was verified at the whole dough level and hence applied at the pixel level [6]. A key point in the method was the use of a T_2-weighted spin-echo sequence and the absence of significant transverse relaxation time changes during proving. One limitation of the method was the omission of heat and mass transfer, which often takes place on an industrial scale, whereas, together with porosity, they may affect MR parameters, particularly magnetic moment, T_1 and proton chemical shift (PCS). Temperature mapping of proved (fermented) dough would make it possible to correct porosity mapping for the temperature effect. Above all, temperature mapping would permit more thorough modelling of bubble inflation or the collapse of bread dough for which temperature is a driving parameter.

T_1, the apparent diffusion coefficient and PCS are temperature-sensitive MR parameters [10] that are most promising for MR temperature mapping. PCS is currently accepted as the method of choice for MR thermometry in homogeneous media [11-13] as it does not suffer from any physical or chemical structure dependency and can give promising results even at low magnetic field [14-15]. However, in addition to the sensitivity of this method to magnetic field drift due to scanner instability, the bubbles in fermented dough generate local susceptibility artefacts, which would also induce phase variations. On the other hand, diffusion measurements are technically demanding in terms of fast and strong gradients and they are not relevant for products with low T_2 such as dough ($T_2 = 20 - 50\ ms$). Furthermore, temperature mapping based on the apparent diffusion coefficient would require a long acquisition time because rapid imaging (*EPI*) is not suitable in the case of dough which presents a high concentration of air bubbles. We therefore chose in our investigation to use T_1 for temperature measurements as it is not sensitive to the above phenomena and technical limitations. Moreover, T_1 measurements are well suited to the studies at low magnetic field (0.2 T

in the present study), and to the study of dough processes during which T_1 does not evolve consecutively to the changes in the molecular structure through reactions such as chilling. Classical determination of T_1 is based on spin echo (SE) sequences with incremental repetition times or inversion–saturation (*IS*) –recovery (*IR*) methods, but their excessively time-consuming nature make them unsuitable for dynamic applications. Low T_2 relaxation time and local susceptibility in dough prevent the use of fast imaging techniques such as turbo-FlASH (fast low angle shot) [16-17] or EPI [18] sequences for T_1 estimation. One recent relatively rapid method for T_1 mapping known as *TOMROP* (T One by Multiple Read-Out Pulses) [19-20] is based on a series of *FLASH* images acquired during the recovery period following 180° pulses, where each line of k space is sampled following the inversion pulse. This method permits calculation of an effective relaxation time T_1^* that by choosing suitable experimental conditions yields the real T_1 [21]. On the other hand, the variable flip angle method investigated by a number of authors (e.g. [22-23]) calculates T_1 with an accuracy similar to that of IR and SR techniques, but with a significant decrease in the acquisition time. The sequence involves establishing spoiled steady state followed by collection of spoiled gradient echo (*SPGR*) images over a range of flip angles. This generates a signal curve that depends on T_1 and which can be linearized, allowing for fast T_1 determination. Several authors have shown that the three dimensional variable flip angle gradient-recalled echo (3D *GE*) technique to obtain the true T_1 value was preferable to the variable flip angle 2D *GE* for which computational modelling of slice-selective radiofrequency excitation is necessary to correct for nonrectangular slice profiles [24-25]. Furthermore, it has been shown that the accuracy obtained using multiple flip angles can be achieved using just two optimized angles, with corresponding reduction in the acquisition time [26]. The uncertainty on T_1 from such a simplified method was recently derived from the theory of propagation of uncertainty [27]. Similarly, in order to achieve faster T_1-estimation, the spin echo sequence can be used with an optimized pair of repetition times. Imran *et al.* [28] have reported a study in which two-point spin echo and gradient echo methods with optimization criteria were compared and applied for the T_1 mapping of the brain.

MRI temperature mapping based on T_1 or PCS has been evaluated in the food science and engineering fields for ohmic [29-30] and microwave heating [31-32] of water-rich systems, such as gels and liquid-particulate models. However, no MRI methods have been reported quantifying temperature in food characterised by high porosity level and low signal to noise ratio such as bread dough.

The purpose of this study was to evaluate different T_1-weighted MRI temperature mapping methods by 0.2T MRI, to optimize their parameters and to apply these methods to fermented dough during the chilling process. Rather than using time-consuming T_1 mapping methods based on many incremented repetition times or flip angles, temperature mapping methods based on two-point sequences were tested. Different repetition times and flip angles of the 2D and 3D GE sequences and different repetition times of the 2D spin echo sequence were tested, yielding the calculation of different MRI T_1-weighted parameters. Temperature was calibrated against these MRI parameters. These different parameters were compared and a compromise between minimum acquisition time and minimum uncertainty was sought. For the estimation of uncertainties, an analytical investigation of the error propagation was performed according to the guide to the expression of uncertainty measurement[33]. These results were validated experimentally. At last, temperature mapping in pre-fermented dough during chilling prior to freezing was achieved with the best method found and compared locally to measurements by optical fiber.

2 Theoretical aspects

The aim of this section is to present a model of the MRI signal as a function of temperature; this model will then serve for the propagation of errors through each measurement process and the uncertainty of temperature measured by MRI will be estimated.

2.1 Signal modelling and temperature dependency of relaxation parameters

According to Bloch equations, and assuming a mono-exponential relaxation in dough, the MRI signal represented by the grey level (GL_{X_i}) can be modelled for SE (with flip angles of 90° and 180°) and GE, respectively [34] as:

$$GL_{TR_i} = M_o\, e^{\frac{-TE}{T_2}} \left(1 - 2\, e^{\frac{-\left(TR_i - \frac{TE}{2}\right)}{T_1}} + e^{\frac{-TR_i}{T_1}}\right) \quad (1.)$$

$$GL_{\alpha_i} = M_o\, e^{\frac{-TE}{T_2^*}} \sin(\alpha_i) \frac{1 - e^{\frac{-TR}{T_1}}}{1 - \cos(\alpha_i)\, e^{\frac{-TR}{T_1}}} \quad (2.)$$

where M_o is the proton density of the matter under study, weighted by the signal gain, TE the echo time, TR the repetition time, α the flip angle, T_2 and T_1 the transversal and longitudinal relaxation times respectively. M_o, T_2 and T_1 vary with temperature. The index X_i refers to different protocols of measurement, making $X = TR$ or $X = \alpha$ to vary in accordance with the methods described below.

The aim of the present study is to relate the following MRI parameters (SR_{TR}, $\hat{E}_1$ and SR_α; Eqs. (3-5)), depending on the method employed, to temperature. P was used as a generic name for all these MRI parameters. For the method based on a SE sequence with variable repetition time (TR), the parameter is defined as:

$$SR_{TR} = \frac{GL_{TR_1}}{GL_{TR_2}} \quad (3.)$$

where GL_{TR_1} and GL_{TR_2} are the grey levels (signals) of the MRI images acquired with the SE sequence at the low and high TR, respectively. The symbol SR refers to the signal ratio.

For the method based on a GE sequence with variable α, two parameters are calculated. Firstly, $\hat{E}_1$ is defined as an estimate of the slope of the linear relationship between $GL_\alpha / \sin\alpha$ and $GL_\alpha / \tan\alpha$ according to Deoni *et al.* [26]:

$$\hat{E}_1 = \frac{\frac{GL_{\alpha 2}}{\sin\alpha_2} - \frac{GL_{\alpha 1}}{\sin\alpha_1}}{\frac{GL_{\alpha 2}}{\tan\alpha_2} - \frac{GL_{\alpha 1}}{\tan\alpha_1}} \quad (4.)$$

where α_1 and α_2 are the low and high flip angles, respectively, and $GL_{\alpha 1}$ and $GL_{\alpha 2}$ the grey levels in the images acquired with these angles, respectively. Secondly, the signal ratio is calculated directly:

$$SR_\alpha = \frac{GL_{\alpha 1}}{GL_{\alpha 2}} \quad (5.)$$

Combining Eqs (1-2) into Eqs (3-5), $M_o\, e^{\frac{-TE}{T_2}}$ simplifies and Eqs (3-5) become:

$$SR_{TR} = \frac{1 - 2\,e^{\frac{-\left(TR_1 - \frac{TE}{2}\right)}{T_1}} + \sigma_1}{1 - 2\,e^{\frac{-\left(TR_2 - \frac{TE}{2}\right)}{T_1}} + \sigma_2} \quad (6.)$$

$$\hat{E}_1 = \frac{\lambda_2 - \lambda_1}{\cos(\alpha_2)\lambda_2 - \lambda_1} \quad (7.)$$

$$SR_\alpha = \frac{\sin(\alpha_1)\lambda_1}{\sin(\alpha_2)\lambda_2} \quad (8.)$$

where $\sigma = e^{\frac{-TR}{T_1}}$, $\lambda_i = \frac{1-\sigma}{1-\cos(\alpha_i)\sigma}$ and $\sigma_i = e^{\frac{-TR_i}{T_1}}$.

MRI signals as well as P parameters are related to temperature (T) through M_o, T_2 and T_1.

T_1 temperature dependency can be modelled by an Arrhenius law:

$$T_1 = A\ e^{-\frac{B}{T}} \tag{9.}$$

where A and B are parameters specific to dough.

T_2 can be also modelled by the Arrhenius law and M_O by the Curie's law ; given that T_2 in dough varies little with temperature between the initial freezing temperature and 40°C, these two functions are approximated by a single Curie's law :

$$M_O\ e^{\frac{-TE}{T_2}} = \frac{C}{T} \tag{10.}$$

The measurement of T requires its expression as a function of SR_{TR}, A, B, TR_1 and TR_2 for the method based on SE sequence and of SR_α or $\hat{E}_1$, A, B, α_1 and α_2 for the method based on GE sequence. Inversion of such a function is not feasible, and so is the analytical error propagation through the two models (Bloch equations and Arrhenius law). As a first approximation, a linear approximation is proposed – it will be referred as hypothesis H_1 in the remainder of the paper:

$$P = aT + b \tag{11.}$$

Such hypothesis is valid when the mechanisms affecting the MRI signal conceptualized in the Bloch equations are taken into account only (Figure 1). This hypothesis would merit experimental verification when more mechanisms are involved.

2.2 Error propagation through the process of measurement

As proposed by the Guide to the expression of the Uncertainty in Measurement –GUM [33], the uncertainty of a quantity Y, defined as the function f of m variables $X_j, j \in [1,m]$, is given by:

$$u_Y{}^2 = \sum_{j=1}^{m}\left(\frac{\partial f}{\partial X_j} u_{X_j}\right)^2 + 2\sum_{j=1}^{m-1}\sum_{k=j+1}^{m}\frac{\partial f}{\partial X_j}\frac{\partial f}{\partial X_k} u_{X_j, X_k} \tag{12.}$$

where u_{X_j} is the uncertainty of X_j, and u_{X_j, X_k} the covariance between variables X_j and X_k.

Applying Eq. (12) to Eq. (11) gives the uncertainty of T noted u_T, as:

$$u_T = \sqrt{\left(\frac{1}{a}\right)^2 u_P^2 + \left(-\frac{P-b}{a^2}\right)^2 u_a^2 + \left(-\frac{1}{a}\right)^2 u_b^2 + 2\left(-\frac{P-b}{a^2}\right)\left(\frac{1}{a}\right) u_{a,b}} \quad (13.)$$

where u_P, u_a and u_b are the uncertainties of the MRI parameter used, the slope and the intercept of the y-axis of the calibration line between the MRI parameter and temperature, respectively.

The second to fourth terms in the right-handed part of the above equation represent the contribution of the modelling step to the final uncertainty of temperature:

$$C_{\text{model}} = \left[\left(-\frac{P-b}{a^2}\right)^2 u_a^2 + \left(-\frac{1}{a}\right)^2 u_b^2 + 2\left(-\frac{P-b}{a^2}\right)\left(\frac{1}{a}\right) u_{a,b}\right] / u_T^2 \quad (14.)$$

C_{model} evaluates both the quality (in terms of uncertainty) of calibration data and their closeness to the selected model. Covariance can be estimated by:

$$u_{a,b} = -\bar{T} u_a^2 \quad (15.)$$

where $\bar{T}$ is the temperature averaged over a given set of experimental data.

The first term in the right-handed part of Eq. (13) represents the contribution of P to the final uncertainty of temperature:

$$C_{\text{P}} = \frac{u_P^2}{a^2 u_T^2} \quad (16.)$$

The higher the slope or the lower the uncertainty of the P parameter, the lower the final uncertainty of temperature (Figure 1).

In order to simplify the theoretical approach (section 2.4), the contribution of the modelling step to the temperature uncertainty is neglected (which will be referred as hypothesis H_2 in the remainder), and only the first term is used:

$$u_T = \left|\frac{1}{a}\right| u_P \quad (17.)$$

Note that the experimental study will also aim at validating the hypothesis H_2.

a in Eq. (17) can be obtained by deriving P according to temperature using Eqs (6-8):

$$a = \frac{dP}{dT} \tag{18.}$$

Such derivation was performed under Maple® using Eqs (6-8) and Eq. (9). a was function of TR_1, TR_2, TE, A, B, T for $P = SR_{TR}$ and α_1, α_2, TR, A, B, T for $P = SR_{\alpha}, \hat{E}_1$.

u_P used in Eq. (17) was estimated by applying Eq. (12) to Eqs. (3-5) and assuming no correlation between the MRI signal acquired with different acquisition parameters:

$$u_{SRTR} = \sqrt{\left(\frac{1}{GL_{TR2}}\right)^2 \times u_{GL_{TR1}}^2 + \left(-\frac{GL_{TR1}}{GL_{TR2}^2}\right)^2 \times u_{GL_{TR2}}^2} \tag{19.}$$

$$u_{\hat{E}_1} = \sqrt{\begin{aligned} &\left[-\frac{1}{\sin(\alpha_1)W} + \frac{Z}{W^2\tan(\alpha_1)}\right]^2 u_{GL_{\alpha_1}}{}^2 \\ &+ \left[\frac{1}{W\sin(\alpha_2)} - \frac{Z}{W^2\tan(\alpha_2)}\right]^2 u_{GL_{\alpha_2}}{}^2 \\ &+ \left[\frac{GL_{\alpha_1}\cos(\alpha_1)}{\sin(\alpha_1)^2 W} - \frac{ZGL_{\alpha_1}\left(1+\tan(\alpha_1)^2\right)}{W^2\tan(\alpha_1)^2}\right]^2 u_{\alpha_1}{}^2 \\ &+ \left[-\frac{GL_{\alpha_2}\cos(\alpha_2)}{W\sin(\alpha_2)^2} + \frac{ZGL_{\alpha_2}\left(1+\tan(\alpha_2)^2\right)}{W^2\tan(\alpha_2)^2}\right]^2 u_{\alpha_2}{}^2 \end{aligned}} \tag{20.}$$

with:

$$\begin{cases} W = \dfrac{GL_{\alpha_2}}{\tan(\alpha_2)} - \dfrac{GL_{\alpha_1}}{\tan(\alpha_1)} \\ Z = \dfrac{GL_{\alpha_2}}{\sin(\alpha_2)} - \dfrac{GL_{\alpha_1}}{\sin(\alpha_1)} \end{cases} \tag{21.}$$

$$u_{SR_{\alpha}} = \sqrt{\left(\frac{1}{GL_{\alpha_2}}\right)^2 \times u_{GL_{\alpha_1}}^2 + \left(-\frac{GL_{\alpha_1}}{GL_{\alpha_2}^2}\right)^2 \times u_{GL_{\alpha_2}}^2} \tag{22.}$$

where $u_{GL_{X_i}}$ is the uncertainty of the signal in given acquisition conditions i and u_α is the uncertainty of the flip angle. GL_{X_i} used in Eqs (19-22) were calculated by combining Eqs. (1-2) and (9-10). GL_{X_i} was function of TR_i, TE, A, B, C, T when using the SE sequence and α_i, TR, A, B, C, T when using the GE sequence.

2.3 Numerical applications for estimation of u_T

Numerical applications concerned the MRI parameters SR_{TR} and SR_α only.

Temperature was set at 273.15 K (0° C); the results could be extrapolated to other values of temperature.

Parameters A and B (Eq. 9) were adjusted according to transverse relaxation times obtained on dough prepared in the same way as the dough studied here (data not reported) and were estimated at 3361 and 941.1 K respectively. C (Eq. 10) was adjusted according to the signal acquired by MRI with a SE and GE sequence, with values of parameters given in section 3.3 except for TR, which was five times greater than T_1, and α, which was set at 90° for the GE sequence. C was estimated at 263 551 and 474 493 K for SE and GE sequences, respectively.

TE was set at 8.1 ms for the SE sequence and TR at 50, 100, 300 and 500 ms for the GE sequence. Different duplets of TR_i or α_i were considered and their effect on the estimation of the temperature uncertainty are presented in the next section.

$u_{GL_{X_i}}$ was attributed to noise mainly and estimated from experimental MRI data as detailed in section 3.5. The number of averages in the sequence was set at 4, decreasing the uncertainty by a factor of 2. GL_{X_i} was assumed to be averaged over 25 pixels in the ROI, decreasing the uncertainty by a factor of 5 (see section 3.5). $u_{GL_{TR}} = 4.8\ a.u.$ and $u_{GL_\alpha} = 6.8\ a.u.$ $\forall i$ for SE and GE sequences, respectively.

2.4 Effects of acquisition parameters on uncertainties

The shorter the TR_1, the lower the u_T deduced from the SE method with variable TR (Figure 2), and increasing TR_2 over 300-400 ms did not contribute much to further decreasing the uncertainty of temperature for short TR_1.

u_T deduced from the GE method with variable α was minimized by increasing α_2 up to 90° whatever the TR value. Optimal values of α_1 for minimizing the uncertainty of temperature were between 20 and 30° for $TR \leq 100$ ms and between 30° and 50° for $TR \geq$ 300 ms. These trends are illustrated in Figure 3 with a selection of two extreme values only.

The aim of following experiments was to validate hypotheses H_1 and H_2, and to confirm the above trends regarding u_T.

3 Materials and methods

3.1 Sample preparation and experimental procedure

Dough was prepared with 2000 g wheat flour (Type 55, ash 0.53%, proteins 10.58%, from Moulins Soufflet Pantin, France), 1140 g water (uncontrolled quality), 40 g salt (La Baleine, France), 20 g appropriate baking powder (Puratos, Belgium), and 100 g compressed yeast (l'Hirondelle, Lessafre, France). To avoid time-course changes in porosity, yeast was omitted for calibration purposes, but the mass of water was adjusted to obtain the same final water content as in the yeasted dough. The flour had been stored at -20° C and was defrosted 24 h before the experiment at ambient temperature. The water content of the flour was measured before each new experiment to check any change and was shown to be maintained at 0.14 ± 0.005 $kg.kg^{-1}$ (wet basis). The ingredients were mixed in a special kneader (Moretti Forni, Spiry 8, Italy). They were first

roughly mixed and the aggregates which had stuck to the internal walls of the kneader were removed (<5 min). Dough was then mixed at 100 rpm for 17 min so that the final temperature was 25 ± 1 ° C. Initial water content was determined from three dough samples after oven-drying at 104 ± 1° C for at least 24 h (0.45 ± 0.002 $kg.kg^{-1}$, wet basis).

For the calibration study, glass tubes (11 cm long, internal diameter 2.6 cm) were filled with non-yeasted dough using a compressed air jack in order to limit the incorporation of air at filling and the presence of large gas bubbles in the dough section in MRI images. The tubes were then frozen at -33° C and thawed at 4° C 24h before experiments. After thawing, an optical fiber was placed in the middle of the tube (4.5cm deep) and a second one was positioned close to the internal surface of the tube, at the same depth as the other fiber. The tube was placed in a temperature-controlled environment within the MRI field and the temperature of the environment was increased step by step from -1 to 38° C, with a total of five steps. After each increase in temperature, the core of the sample took 90 min to reach the new thermal equilibrium and only then did MRI acquisition begin. Temperature drift in the calibration samples did not exceed 0.1° C during MRI acquisition. The results are based on a single dough preparation; in order to evaluate the reproductibility of the results, three to four batches of dough were performed for two experimental conditions: with the SE sequence using TR_1 = 100ms and TR_2 = 300 ms and 4 scans, and with the 2D GE sequence using TR =100ms and all values of flip angles.

For the application study (chilling of pre-fermented doughs), 100g of yeasted dough were rolled manually and placed on a plastic plate in a proving chamber (35° C, >95% humidity) until its volume was double (evaluated by a graduated tester of cylindrical shape filled with 25g of dough). Assuming 10% porosity at the end of mixing, doubling the dough volume corresponded to an approximate porosity of 50%, which is the maximum inflation recommended for pre-fermented doughs prior to freezing. At the exit of the proving chamber, an optical fiber was inserted vertically into the dough 2 cm from the bottom of the dough at mid-width. The instrumented roll was then placed within the MRI magnet in a temperature-controlled environment (previously set at -1° C) and MRI sequences were launched in queue. The experiment was performed three times.

3.2 Reference temperature measurements

Temperatures were measured with calibrated optical fibers (Fiso, Quebec, Canada. Fiso FOT-L, diameter 1mm, accuracy ±1° C) and collected using a data logger (Fiso, UMI-8).

3.3 MRI measurement

As temperature, and possibly porosity, may change rapidly during dough processing, it is important to avoid long acquisition times, which would cause both averaging and blurring of images. The limit was initially set at 1min40-1min50 which corresponded to maximum variations in porosity and temperature of 1% (m^3 of gas per 100 m^3 of dough) and 0.3° C, respectively, during chilling of pre-fermented doughs as studied in section 4.2. Although yielding longer acquisition times than this limit value, the values of acquisition parameters such as number of averages or TR were tested in the present study.

The chilling time attributed to the MR images was centered with respect to the sequence duration and calculated as:

$$\begin{cases} t_0 = \dfrac{\delta t}{2} \\ t_k = t_{k-1} + \delta t + \delta t_1 \quad for\ k > 0 \end{cases} \tag{23.}$$

where δt and δt_1 are the acquisition time, and the interval between the end of the k-1th acquisition and the very beginning of the kth acquisition, respectively.

The MR images were acquired on a 0.2T imager (OPEN, Siemens, Erlangen, Germany) with the different sequences described below. The matrix size for all of them was 128 × 128 and the field of view (FOV) was 128 × 128 mm, resulting in a pixel resolution of 1 mm.

3.3.1 Spin echo sequences (SE)

A commercially provided Siemens SE sequence and a home made SE sequence with variable TR were used in the study. The first sequence was applied in the calibration step only and the second sequence in the application step only.

The parameters of the commercially provided Siemens SE sequence were: TE = 8.1 ms, number of averages = 2 or 4, slice thickness = 10mm.

Combination of TR values minimizing the uncertainty of temperature (on the basis of the theoretical approach described above) and the acquisition times were studied only. Because of too long acquisition times relative to the dynamics under study, values of TR higher than 400 ms were discarded. TR values below 100 ms were not studied since the signal to noise ratio may not be sufficient for the application step. TR values of 100, 200, 300 and 400 ms were tested and three different SR_{TR} presenting a theoretical uncertainty of temperature lower than 5°C (Figure 2) were calculated.

A SE sequence with variable TR was developed to acquire spin echoes at two TR in the same sequence. Each line of the Fourier K-space was acquired alternately for each of the two different T_1-weighted images. The advantage of such a sequence when applied to products with time-dependent geometry is to eliminate the spatial shift between two images due to the time difference between the successive acquisitions of classical SE images. It was previously established that the signal obtained from this sequence was close to those measured from the classical T_1-weighted Siemens SE sequence. The slice thickness and the number of averages were the same as the Siemens SE sequence. TE was 7.7 ms, and TR were 100 and 300 ms.

3.3.2 Gradient echo sequences (GE)

Three- (3D) and two- (2D) dimensional RF spoiled GE sequences were tested for this study.

The parameters of the 3D GE sequence were: TE = 12 ms, number of averages = 1, slice thickness = 5 mm, number of slices = 8, slab thickness = 40 mm, and different TR were tested (50, 70, 100 and 300 ms). TR below 50 ms were not tested since the signal to noise ratio may not be sufficient for the application step. α was varied (10, 20, 30, 40, 50, 60, 70, 80 and 90°) for each TR value.

The parameters of the 2D GE sequence were: TE = 4 ms, slice thickness = 10 mm. The same TR and α values as for the 3D GE sequence were tested. The number of averages was variable with TR (2, 4, 6, or 8), attempting to minimize the acquisition time while preserving the signal to noise ratio.

Because variations in α did not impact the acquisition time as varying TR in the method based on the SE sequence, the whole range of α values was studied with the aim of fully validating the theoretical calculations presented in Figure 3. For the purpose of comparing the different methods (different P parameters), optimal values of α determined from the theoretical approach will be used only, *i.e.* α_1 = 30° and α_1 = 90° whatever the TR value. The effect of TR will be presented.

3.4 Analysis of MRI images

3.4.1 Calculation of P at the calibration step

A region of interest (ROI) in the dough section containing $n = 25$ pixels (5×5) was then drawn in the central part of the MRI images using the Scilab software and the mean value of GL_{X_i} was calculated. P values were calculated from these data according to Eqs. (3-5). Special care was taken to exclude air bubbles from ROIs.

3.4.2 Calculation of P at the application step

SR_{TR} only will be treated in the section.

Using a home-made programme developed with the Scilab software, the MRI images of the dough roll acquired with the SE sequence during chilling with variable TR were converted into temperature maps.

In order to reduce noise, MRI images were first filtered using average filtering by a 3×3 kernel, followed by a convolution product using a 5×5 matrix. Maps of SR_{TR} were calculated from these images according to Eq. (3). The resulting images were then averaged between the three runs for identical times of acquisition.

This was made possible by essentially identical shapes of dough rolls between the three runs (maximum variation in section was less than 5% in height and less than one pixel in diameter) and by identical dynamics of chilling as evaluated from time-course changes in temperature measured at 2 cm from the bottom of the dough with optical fibers (reproducibility of ± 0.5° C). Dough location in the FOV did vary from one run to another, especially in the horizontal direction, and dough barycentres were therefore translated horizontally prior to averaging.

SR_{TR} was then converted into temperature according to Eq. (11). Note that the calibration curve was determined from images of non-yeasted dough. Preliminary T_1 measurements performed on a 20 MHz (0.47 T) spectrometer (Minispec PC-120, Bruker, Karlsruhe, Germany) with the SR sequence showed a difference in T_1 between yeasted and non-yeasted doughs which was relatively constant whatever the temperature in the range of 0 to 35° C. An additional offset of 0.0244 was therefore applied to the linear calibration curve established from MRI signals of non-yeasted doughs; this was calculated as the difference in SR_{TR} between yeasted dough just at the end of mixing (25° C) and the prediction of Eq. (11) at the same temperature.

Finally, temperature maps were averaged over three consecutive times of acquisition. This last averaging step was motivated by the small time-course changes in temperature as verified by reference temperature measurements (variations less than 1° C, see Results and Discussion section).

A rectangular ROI of 10 pixels high and 4 pixels wide (40 pixels) was placed in the dough at mid-width between 1 to 2 cm from the bottom of the dough, consistently with the location of the head of the optical fiber sensor at 2 cm from the bottom of the dough and the sensor chamber of 1 cm long. Areas of measurement between the optical fiber and MRI were thus comparable.

Despite the low spatial resolution of the MRI images, pre-fermented doughs may present pixels with very low signals due to medium-sized bubbles. In such cases, the result of Eq. (3) was very sensitive to noise and aberrant values of temperature were calculated (deviations between 20 and 200° C from the expected value). Such pixels were therefore not taken into account in the analysis, meaning the omission of a maximum of 5 pixels out 40 selected in the ROI placed between 1 and 2 cm from the bottom.

3.5 Estimation of uncertainty

Experimental uncertainty of T was deduced from Eq. (13).

a and b in Eq. (13) with their associated uncertainties u_a, u_b and $u_{a,b}$, were deduced after application of a linear regression on P experimental data plotted against T using a least mean square method.

u_P was calculated from Eqs (19,20,22) depending on GL_i and/or α_i, and their uncertainties. GL_i was estimated directly from images following instructions detailed in section 3.4.1. α_i was the value of the flip angle used in the protocol of measurement. Calculations of uncertainties on GL_i and α_i are detailed below. As the flip angle variations across the plane of the imaging slice is a result of the inhomogeneity in the RF transmit field (B_1) [35], the flip angle uncertainty was determined from the standard deviation in a ROI placed in a B_1 cartography. This was estimated at 0.6 % of the angle value.

Only the variability due to electronic noise was retained as a contributor to the uncertainty of GL_i. In the case of SNR higher than 5, the uncertainty associated with the signal measured in a single pixel ($n=1$) was estimated as:

$$u_{GL_{X_i},n=1} = \frac{\overline{GL}_{X_i,back}}{\sqrt{\frac{\pi}{2}}} \tag{24.}$$

where $\overline{GL}_{X_i,back}$ is the mean grey level in the background of the image acquired in condition i [36]. As expected, values of uncertainties were found to be constant whatever the TR or α, but varied with the number of averages at the acquisition step. They were also decreased by averaging performed at the image analysis steps:

$$u_{GL_{X_i},n} = \frac{u_{GL_{X_i},n=1}}{\sqrt{n}} = u_{GL_{X_i}} \tag{25.}$$

where $GL_{X_i,n}$ is the grey level averaged over a ROI containing n pixels.

At the calibration step, the absolute uncertainty was $\sqrt{n} = 5$ times less than that associated with a single pixel. Note that such a reduction factor also applies to the uncertainties of P (see Eqs. (19, 22) since u_{GL_i} was independent of TR or α, implying a direct proportionality between $u_{GL_{X_i}}$ and u_P; the same applies to u_T assuming that C_{model} is negligible –see Eqs (13-14). Because the slice thickness for the 3D GE sequence was 5 mm instead of 10 mm for all the other sequences, all the uncertainties calculated for the 3D GE method with variable α were weighted by a factor of 1/2 to be comparable.

At the application step, the consecutive steps of averaging (between $n_1 = 3$ runs, between $n_2 = 3$ consecutive times, between $n_3 = 40$ pixels contained in the ROI, see section 3.4.2) reduced the absolute uncertainty by a factor of 19 compared that associated with a single pixel (Eq. 24). On the other hand, compared to the calibration step, the grey level measured in a pixel was reduced by a factor of more than about 2 (due to porosity, passing from 10% to more than 50%, expressed in m^3 of gas per 100 m^3 of dough). The relative uncertainty of GL_i at the application step was theoretically about half the value obtained at the calibration step for the same number of averages.

4 Results and discussion

4.1 Calibration on non-yeasted dough

4.1.1 SE method with variable TR

SR_{TR} was linear with temperature (Figure 4), with a high determination coefficient (Table 1). There were small differences in slope (±8%) and intercept of the y-axis (±2%) between the three repetitions. However, they were within the range defined by the uncertainties (u_a, u_b). Such differences could be partly explained

by the uncertainty of temperature measured by optical fibers, which is about 1° C. A variation of 1° C on data presented in Figure 4 may greatly affect the slopes of these lines. As expected, the parameters identified were close while acquiring 2 and 4 averages for run 1 (Table 1), the deviation being within the uncertainty of repeatability.

4.1.2 GE method with variable α

4.1.2.1 $\hat{E}_1$

As expected from the theory [26], $\frac{GL_\alpha}{\sin\alpha}$ was linear with $\frac{GL_\alpha}{\tan\alpha}$ for the 3D GE method with variable α, with high determination coefficient values for $TR \leq$ 100 ms (i.e. above 0.99). The slope value decreased with increasing TR and tended to zero at TR=300 ms because the signal varies slowly with angle for long TR. The results obtained at TR=300 ms are therefore not further discussed. The trends at -0.5° C are illustrated in Figure 5.

E_1 is the slope of these straight lines, and was constant with temperature given the small range of temperatures. In the present study E_1 ($\hat{E}_1$ in Eq. (4)) was estimated using two flip angles, for the different temperatures studied. In theory, the greater the difference between these two angles, the better the estimate of $\hat{E}_1$. However, the images acquired with 10° and 20° angles presented too low signal to noise ratio and the signals acquired with these two angles deviated most from the overall linear regression, as shown in Figure 5. Hence, all calculations were made with images acquired with α_1=30° and α_2=90° (Figure 6). The values of the parameters from the linear regression with their uncertainties are reported for different TR in Table 1. $\hat{E}_1$ was linear with temperature, with fairly high determination coefficients. The slope values were low, around 3.10^{-3}, and did not vary with TR to any great extent.

The 2D GE method with variable α did not permit the T_1 estimation from the linearized signal; the relationship between $\frac{GL_\alpha}{\sin\alpha}$ and $\frac{GL_\alpha}{\tan\alpha}$ did not allow calculation of E_1. This is consistent with previous

results reported by Brookers et al. [24]. The principal reason for this is that for 2D image acquisition the slice profile is not perfectly rectangular and the signal does not correspond to its theoretical value, especially when TR is reduced or α is increased. These findings have not been reported or discussed further.

4.1.2.2 SR_α

Like for $\hat{E}_1$, SR_α was calculated using α_1=30° and α_2=90°. Whatever the –3D or –2D GE method with variable α (Figure 7, Table 1), the SR_α according to temperature was linear, although with slightly worse overall determination coefficients related to those obtained for the two-point SE method (Table 1). For the 3D GE method with variable α, the slope values increased twice when TR decreased from 100 to 50 ms. It must be emphasized that such an effect of TR on the slope was not observed for previous parameters. For the 2D GE method with variable α, the determination coefficients were better overall than for 3D. Slope values also increased with decreasing TR, but to a lesser extent (by about 60% for the same range of TR values as for the 3D GE method with variable α).

The different MRI parameters selected (P) varied quite linearly with temperature, validating hypothesis H_1.

4.1.3 Estimation and propagation of uncertainties

Eq. (13) could be applied to evaluate the uncertainty on temperature. The values of regression parameters and their uncertainties evaluated in the previous sections and reported in Table 1 were used for this purpose.

u_P was estimated at -0.5° C for the different sequences tested and their parameters and reported in Table 1. Contribution of P to temperature uncertainty (C_P in Eq (16)) is also reported in Table 1 and will be discussed overall with the model contribution (Eq (14)). The final uncertainty to be computed was that of temperature. u_T was calculated from Eq. (13) and calculations at about -0.5° C are also reported in Table 1.

It must be emphasized that the temperature uncertainty obtained with SR_{TR} increased with temperature. The best fit was:

$$u_T = g\,T^2 + h\,T + i \qquad (26.)$$

where $g = 0.0025°C^{-1}$, $h = -0.0267$ and $i = 16.383°C$ ($R^2 = 0.9789$).

For $\hat{E}_1$, u_T was constant with temperature, whereas it increased with temperature for SR_α following Eq. (26): $g = 0.0049°C^{-1}$, $h = 0.1199$ and $i = 17.863°C$ for 3D GE sequence ($R^2 = 0.9937$) and $g = 0°C^{-1}$, $h = 0.135$ and $i = 23.368°C$ ($R^2 = 0.9854$) for 2D GE sequence. Despite these variations, the trends discussed below can be extrapolated to higher temperatures.

It can be seen from the results in Table 1 that the modelling step (C_{model}) did not significantly contribute to the temperature uncertainty compared to the P parameter (C_P), thus validating hypothesis H_2. This meant that Eq. (17) can be applied to estimate u_T with two main factors, *i.e.* the slope value, a, and the uncertainty of P. Returning to the results presented in section 4.1, this also meant that the imperfections noted for some linear regressions were not significant in relation to the high level of uncertainty attributed to P.

For the 2D GE method with variable α, the qualitative effect of α on u_T as predicted by the theory was well reproduced experimentally. Some quantitative discrepancies were observed although the values were close. All this is illustrated and discussed for TR = 50 ms (Figure 8). u_T was higher for lower values of α_2 and asymptotically tended to 5° C for high values of α_2 instead of 2.5°C estimated theoretically. When α_2>40°, α_1 = 20° minimized u_T; such optimum was reported for slightly lower values of α_2 (30-35°) in the theoretical considerations (Figure 3). Moreover, these experimental results supported the only calculation of SR_α for α_1=30° and α_2 =90° (see Material and Methods section, and Table 1).

Focusing on SR_α calculated for 4 averages and TR= 70, 100 and 300 ms, both the slope and the uncertainty of P increased with decreasing TR. Poor results at $TR \geq 300$ ms were due to very low slope values (~10^{-4}), indicative of a sensitivity limit. However, since shorter acquisition times (*i.e.* lower TR) also

produced lower uncertainties of temperature, findings at $TR \geq 300$ ms were not exploited further. For $TR \leq 100$ ms, decreasing TR increased the slope to a higher extent than u_P [see Eq. (17)] yielding the lowest uncertainty on T for the lowest TR.

At equal acquisition times, sequences with lower TR can be run with a higher number of averages, resulting in a higher signal to noise ratio and lower uncertainty of P. Indeed, the number of averages can be increased from 4 to 8 and 6 at TR=50 ms and 70 ms, respectively. Under these conditions, temperature uncertainty became 2.7 and 3.2°C respectively. TR=50 ms and 8 averages were retained as the best method for the 2D GE sequence with variable α.

For the SE method with variable TR, for 4 averages lower uncertainties for TR_1 =100 ms rather than 200 ms (Table 1) were consistent with the theoretical calculations presented in Figure 2. Calculations reported in Table 1 showed that this result could be attributed to a smaller slope, reduced by a factor of at least two when passing from TR= 200 to 100 ms. There was little difference in temperature uncertainty when using TR_2 = 300 or 400 ms, which was again consistent with Figure 2. Some quantitative discrepancies were noted, although small *e.g.* 1.9° C calculated by theory against 2.4-2.8° C calculated from experimental data at TR_2 =300 ms and TR_1 =100 ms; the same factor between simulated and experimental uncertainties of temperature was observed with other values of TR_1 and TR_2. This could be explained by the under-estimation of P using Bloch equations and Arrhenius law, as noticeable when comparing Figure 1 and 4 for the same values of TR_1 and TR_2 (100 and 300 ms respectively).

The smallest TR_2, *i.e.* 300 ms, was therefore selected, yielding a shorter acquisition time. Thus to reach an acquisition time of about 1min40, with a SR_{TR} using TR_1 =100 ms and TR_2 =300 ms, the number of averages was decreased to 2, giving a final experimental temperature uncertainty of 3.3° C.

For the 3D GE method with variable α (SR_α), both the slope and the uncertainty of P increased with decreasing TR. The relatively high value of the slope at TR=50 ms counterbalanced the increase in u_P and yielded the lowest uncertainty of temperature. TR = 50 ms was therefore retained for the 3D GE sequence,

keeping the number of averages (1) unchanged since the acquisition time was already in the desired range (1min40-50). $\hat{E}_1$ did not give better results than SR_α at even values of TR (Table 1).

To conclude, the sequences implemented to obtain comparable acquisition times produced the temperature uncertainty of 1.8, 2.7 and 3.3° C for the SR_α calculated with the 3D GE sequence, the 2D GE sequence and the SR_{TR} calculated with SE sequence, respectively. Despite the better results obtained using the 2D and 3D GE sequences, the SR_{TR} with the SE sequence was retained for the application step because of its lower sensitivity to susceptibility than GE sequences. Finally, it must be emphasized that in the case of chilling of unfermented doughs (low porosity levels), MRI parameters $\hat{E}_1$ and SR_α obtained with the 3D sequence would be more recommended on the basis of temperature uncertainty (Table 1).

4.2 Application: chilling of pre-fermented doughs

Following the procedure described in the Materials and Methods (section 3.1), small samples of dough (1 cm^3) were prepared and fermented in tubes within the spectrometer used for preliminary T_1 measurements (see section 3.4.2). Chilling was controlled to obtain a linear decrease in temperature in the sample, with the cooling rate between -0.6 and -15.0° $C.min^{-1}$. The results showed that T_1 decreased linearly with temperature and was relatively independent of the cooling rates in the range tested (data not shown). It was also verified from time-temperature curves that the cooling rates at different positions in the dough roll between the surface and core under MRI conditions (-0.4 to -5.3° $C.min^{-1}$) were within the range tested under NMR conditions. All this meant that variations in T_1 due to changes in composition under the fermentation process could be neglected during the chilling stage and that temperature only affected T_1.

Time-course changes in temperature measured at 2 cm from the bottom of the dough (Figure 9) were in good agreement between MRI and the reference method (optical fiber). Standard deviations in dough temperature measured by MRI were twice higher than that reported for the calibration step (7.0° C in average versus 3.3° C). The reverse order was expected since the signal to noise ratio at the application step was half that at the calibration step (see Materials and Methods); the increase in standard deviation was mainly attributed to the

reproducibility between runs (dough temperatures during chilling were averaged over three runs) and the presence of the temperature gradient (questioning the validity of temperature uniformity on averaging between successive images or adjacent pixels (ROI) in the same image), each source contributing equally to the final uncertainty of temperature.

Spatial changes in dough temperature as assessed by MRI during chilling are presented in Figure 10. As expected, heat transfer proceeded rapidly where the surface was in direct contact with air under convection (top surface) and more slowly on contact with the plastic plate (bottom) which offered a greater resistance to heat transfer; this implied that the coldest point moved from the barycentre of the dough roll to the bottom, near the plate. Smooth iso-temperature lines (*i.e.* smooth transitions between colours in Figure 10) might have been expected, but were not observed due to the relatively high level of noise. Nevertheless, satisfactory denoising of data can be achieved using the procedure retained for data presented in Figure 9 (with additional averaging over 40 pixels), an alternative which would still allow spatially-resolved monitoring of temperature in three distinct regions along a given "radius" of the dough roll.

5 Conclusion

In this study, 2D-SE, 2D-GE and 3D-GE two-point T_1-weighted MRI methods were evaluated in order to maximise the accuracy of temperature mapping in dough. Theoretical uncertainties were calculated according to the theory of uncertainty propagation using a model of the MRI signal as a function of temperature. The optimal parameters of the methods that minimised the temperature uncertainty were determined and compared to the experimental results obtained with low-field MRI.

Some discrepancies were reported between experimental and theoretical values of temperature uncertainties; however, experimental and theoretical trends with varying parameters agreed to a large extent, for both SE and GE methods. This in-depth experimental study permitted full validation of the mathematical model relating the MRI parameters to temperature, based on linear assumption, which is a requirement for a theoretical approach to uncertainty propagation. It also made it possible to almost overlook the contribution

of data fitting to the final temperature uncertainty which greatly simplified the theoretical approach. This may however remain specific to the case study chosen with a low sensitivity of the MRI parameters to temperature. As a consequence, optimisation of the acquisition parameters for further applications can be mainly based on a theoretical approach accompanied by simplified experimental validation. A step of experimental validation remains unavoidable in many cases since T_1 may not only vary with temperature but also with bio-chemical/structural changes specific to the food under concern and the associated process.

The final choice also took into consideration the acquisition time which should for the studied process be comprised between 1min40-50 for limited changes of temperature and porosity with time. All the methods studied with comparable acquisition times minimised the temperature uncertainty to the similar extent, with the 3D sequence (SR_α) better than the other ones. The 2D-SE method was chosen for further applications on pre-fermented dough because of its lower sensitivity to susceptibility differences in porous dough. However, the method chosen may be reconsidered for unfermented dough.

Data from temperature maps of pre-fermented doughs were averaged over a group of adjacent pixels and successive acquisitions in order to reduce the uncertainty of measurement. This result suggested the use of lower matrix size in further applications, which will also decrease the acquisition time. Although in a complex way, the use of higher field could also improve the signal to noise ratio and thus decrease the uncertainty of measurement, but it favours the artefacts of magnetic susceptibility. This step requires an experimental validation following the method proposed in this paper. The next step of our investigation will be to test the method on MRI scanner operating at.1.5T.

Results of dough temperature mapping during chilling were presented. Temperature changes were in good agreement with local reference measurements. Above all, MRI measurements provided a single spatial assessment of temperature, highlighted in the case of heterogeneous thermal boundary conditions as in the application selected for the present study.

6 Acknowledgement

This study was carried out with financial support from the Commission of the European Communities, FP6, Thematic Area “Food quality and safety”, FOOD-2006-36302 EU-FRESH BAKE. It does not necessarily reflect its views and in no way anticipates the Commission’s future policy in this area.

REFERENCES:

1. Cauvain SP. Dough retarding and freezing. In: Cauvain SP, Young LS, editors. Technology of Breadmaking. First edition ed. London, UK: Blackie Academic & Professional; 1998. p 149-179.

2. Lucas T, Grenier A, Collewet G, Davenel A. NMR imaging of dough. In: Webb G, Asakura T, Saito H, Ando I, Krane J, Utz M, Belton PS, Mountford CE, Craik D, Aursand M, editors. Handbook of Modern Magnetic Resonance. Surrey, UK: Kluwer Academic Publishers; 2007. p 1785-1790.

3. Whitworth MB, Alava JM. The imaging and measurement of bubbles in bread doughs. In: Campbell GM, Webb C, Pandiella SS, Nirajan K, editors. Bubbles in Food. St Paul: Eds Eagan Press; 1999. p 221-232.

4. Sutton KH, Simmons LD, Morgenstern MP, Chen A, Crocker TL. Non-invasive examination of gas cell structure in dough using confocal microscopy. 2001; Sydney, Australia. The Royal Australian Chemical Institute.

5. Goetz J, Gross D, Koehler P. On-line observation of dough fermentation by magnetic resonance imaging and volumetric measurements. European Food Research and Technology 2003;217(6):504-511.

6. Grenier A, Lucas T, Collewet G, Le Bail A. Assessment by MRI of Local Porosity in Dough During Proving. Theoretical Considerations and Experimental validation Using a Spin-Echo Sequence. Magn Reson Imaging 2003;21(9):1071-1086.

7. Takano H, Ishida N, Koizumi M, Kano H. Imaging of the fermentation process of bread dough and the grain structure of baked breads by magnetic resonance imaging. J Food Sci 2002;67(1):244-250.

8. van Duynhoven JPM, van Kempen GMP, van Sluis R, Rieger B, Weegels P, van Vliet LJ, Nicolay K. Quantitative assessment of gas cell development during the proofing of dough by magnetic resonance imaging and image analysis. Cereal Chem 2003;80(4):390-395.

9. Bajd F, Sersa I. Continuous monitoring of dough fermentation and bread baking by magnetic resoannce microscopy. Magn Reson Imaging 2011;29:434-442.

10. Rieke V, Butts Pauly K. MR thermometry. J Magn Reson Imaging 2008;27(2):376-390.

11. Bertsch F, Mattner J, Stehling MK, Muller-Lisse U, Peller M, Loeffler R, Weber J, Memer K, Wilmanns W, Issels R, Reiser M. Non-invasive temperature mapping using MRI: comparison of two methods based on chemical shift and T1-relaxation. Magn Reson Imaging 1998;16(4):393-403.

12. Bos C, Lepetit-Coiffé M, Quesson B, Moonen CTW. Simultaneous Monitoring of Temperature and T1: Methods and Preliminary Results of Application to Drug Delivery Using Thermosensitive Liposomes. Magn Reson Med 2005;54:1020-1024.

13. DePoorter J, DeWagter C, De Deene Y, Thomsen C, Stahlberg F, Achten E. Noninvasive MRI Thermometry with the Proton Resonance Frequency (PRF) Method: In Vivo Results in Human Muscle. Magn Reson Med 1995;33:74-81.

14. Grimault S, Lucas T, Quellec S, Mariette F. Quantitative measurements of temperature by proton resonance frequency shift at low field: a general method to correct non-linear spatial and temporal phase deformations. J Magn Reson 2004;170:79-87.

15. Sinha S, Oshiro T, Sinha U, Lufkin R. Phase Imaging on a 0.2-T MR Scanner: Application to Temperature Monitoring During Ablation Procedures. J Magn Reson Imaging 1997;7:918-928.

16. Blüml S, Schad LR, Stepanow B, Lorenz WJ. Spin-Lattice Relaxation Time Measurements by Means of a TurboFLASH Technique. Magn Reson Med 1993;30:289-295.

17. Nekolla S, Gneiting T, Syha J, Deichmann R, Haase A. T1 Maps by K-Space Reduced Snapshop-FLASH MRI. J Comput Assist Tomo 1992;16(2):327-332.

18. Clare S, Jezzard P. Rapid T1 Mapping Using Multislice Echo Planar Imaging. Magn Reson Med 2001;45:630-634.

19. Brix G, Schad LR, Deimling M, Lorenz WJ. Fast and precise T1 imaging using a TOMROP sequence. Magn Reson Imaging 1990;8(4):351-356.

20. Peller M, Reinl HM, Weigel A, Meininger M, Issels RD, Reiser M. T1 Relaxation Time at 0.2 Tesla for Monitoring Regional Hyperthermia: Feasibility Study in Muscle and Adipose Tissue. Magn Reson Med 2002;47:1194-1201.

21. Pickup S, Wood AKW, Kundel HL. A Novel Method for Analysis of TOMROP Data. J Magn Reson Imaging 2004;19:508-512.

22. Homer J, Beevens MS. Driven-equilibrium single-pulse observation of T1 relaxation. A re-evalution of a rapid "new" method for determining NMR spin-lattice relaxation times. J Magn Reson Imaging 1985;63:287-297.

23. Wang HZ, Riedered SJ, Lee JN. Optimizing the precision in T1 relaxation estimation using limited flip angles. Magn Reson Med 1987;5:399-410.

24. Brookes JA, Redpath TW, Gilbert FJ, Murray AD, Staff RT. Accuracy of T1 measurement in dynamic contrast-enhanced breast MRI using two- and three-dimensional variable flip angle fast low-angle shot. J Magn Reson Imaging 1999;9(2):163-171.

25. Parker GJM, Barker GJ, Tofts PS. Accurate Multislice Gradient Echo T1 Measurement in the Presence of Non-ideal RF Pulse Shape and RF Field Nonuniformity. Magn Reson Med 2001;45:838-845.

26. Deoni SCL, Rutt BK, Peters TM. Rapid Combined T1 and T2 Mapping Using Gradient Recalled Acquisition in the Steady State. Magn Reson Med 2003;49:515–526.

27. Schabel MC, Morrell GR. Uncertainty in T-1 mapping using the variable flip angle method with two flip angles. Phys Med Biol 2009;54(1):N1-N8.

28. Imran J, Langevin F, Saint-Jalmes H. Two-point method for T1 estimation with optimized gradient-echo sequence. Magn Reson Imaging 1999;17(9):1347-1356.

29. Ruan R, Chen P, Chang K, Kim HJ, Taub IA. Rapid food particle temperature mapping during ohmic heating using FLASH MRI. J Food Sci 1999;64(6):1024-1026.

30. Ye XF, Ruan R, Chen P, Chang KH, Ning K, Taub IA, Doona C. Accurate and fast temperature mapping during ohmic heating using proton resonance frequency shift MRI thermometry. J Food Eng 2003;59(2-3):143-150.

31. Nott KP, Hall LD. Validation and cross-comparison of MRI temperature mapping against fibre optic thermometry for microwave heating of foods. Int J Food Science Technol 2005;40(7):723-730.

32. Knoerzer K, Regier M, Hardy EH, Schuchmann HP, Schubert H. Simultaneous microwave heating and three-dimensional MRI temperature mapping. Innovative Food Science & Emerging Technologies 2009;10(4):537-544.

33. ISO standards. Guide to the Expression of Uncertainty of Measurement Genève, Switzerland: ISO; 1993. 101 p.

34. Bernstein MA, King KF, Zhou XJ. Handbook of MRI Pulse Sequences: Elsevier Academic Press; 2004. 1017 p.

35. Stollberger R, Wach P. Imaging of the active B-1 field in vivo. Magn Reson Med 1997;38(2):246-251.

36. Gudbjartsson H, Patz S. The Rician Distribution of Noisy MRI Data. Magn Reson Med 1995;34(6):910-914.

Figure captions

Figure 1. P as a function of temperature calculated from Bloch equations (Eq. 1) and Arrhenius law (Eq. 9); numerical applications for $P = SR_{TR}$ consistently with the application study, temperature of [0, 40°C], A=3361, B = 941.1 K for dough, TR_1 = 100ms, TR_2 = 300ms, TE = 8.1 ms. Temperature uncertainty propagation (u_T) was superimposed, considering the uncertainty of the MRI parameter (u_P) only and its conversion through the calibration curve. a is the slope between P and temperature.

Figure 2. Theoretical uncertainty of temperature deduced from SR_{TR} as a function of TR_1 and TR_2. Experimental duplets (TR_1, TR_2) are marked with crosses.

Figure 3. Theoretical uncertainty of temperature deduced from SR_α as a function of α_1 and α_2 at TR=50 ms and 300 ms.

Figure 4. SR_{TR} as calculated from SE versus temperature in non-yeasted dough for different TR values (0.5° C >T>-0.8° C, number of averages = 4). Uncertainty due to noise was lower than 6% (Table 1).

Figure 5. $\frac{GL_\alpha}{\sin\alpha}$ versus $\frac{GL_\alpha}{\tan\alpha}$ for the 3D GE sequence. T = -0.5° C, number of averages = 1. Each experimental point was accompanied by the value of α, expressed in degrees.

Figure 6. $\hat{E}_1$ versus temperature for the 3D GE sequence for different TR. α_1 = 30°, α_2 =90°, number of averages = 1. Uncertainties due to noise were 15, 19 and 29% for TR = 50, 70, 100 ms, respectively (Table 1).

Figure 7. SR_α versus temperature, as calculated for the 3D GE sequence (number of averages = 1) and the 2D GE sequence (number of averages = 4). α_1 = 30°, α_2 =90°.

Figure 8. Experimental uncertainty of temperature deduced from SR_α as a function of α_1 and α_2 at TR=50 ms and 4 averages.

Figure 9. Time-course changes in temperature (average between three runs) at 2 cm from the bottom during chilling of pre-fermented doughs placed in ventilated air at -1° C: comparison between the MRI method (SR_{TR} with the SE sequence) and the reference method (optical fiber).

Figure 10. MRI maps of temperature obtained from SR_{TR} with the SE sequence during chilling of pre-fermented doughs placed in ventilated air at -1° C. Temperature was averaged locally over three runs and is represented in false colours following the bar scale in ° C at the right hand of the Figure. First image was acquired at 3 min, each image being separated by 5 min from left to right.

Table 1. Comparison of methods (using different MRI sequences and acquisition parameters) for measuring local temperature: values of acquisition parameters, values of signal to noise ratio calculated from images of P, values of parameters a and b from linear regression between P and T and the associated uncertainties on these parameters, P uncertainties u_P calculated from Eqs (19, 20, 22) and temperature uncertainties u_T from Eq. (13), with the different contributions C_{model} and C_P calculated according to Eqs (14) and (16). u_T were calculated after averaging between n = 25 data. For each MRI parameter P, the minimum uncertainty reached fro an acquisition time of about 1min40 was presented with a grey background.

Figure1

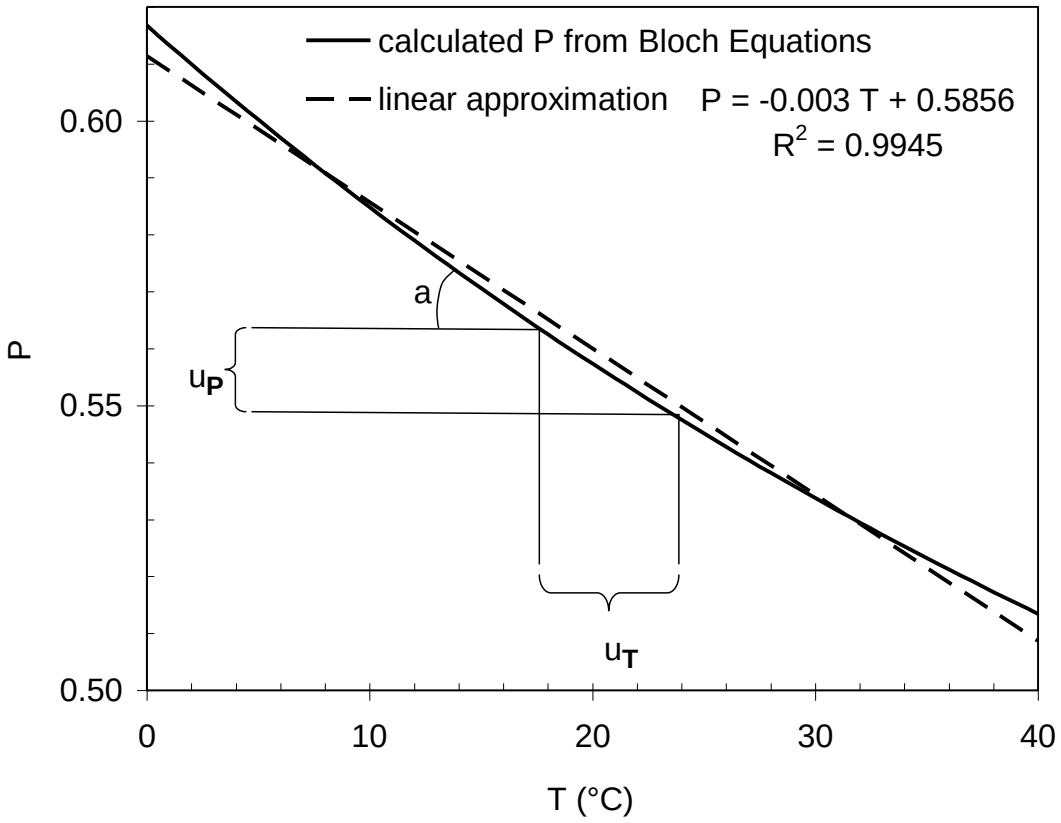
calculated P from Bloch Equations
linear approximation P = -0.003 T + 0.5856
R2 = 0.9945
a
uP
uT
P
0.60
0.55
0.50
0
10
20
30
40
T (°C)

Figure2

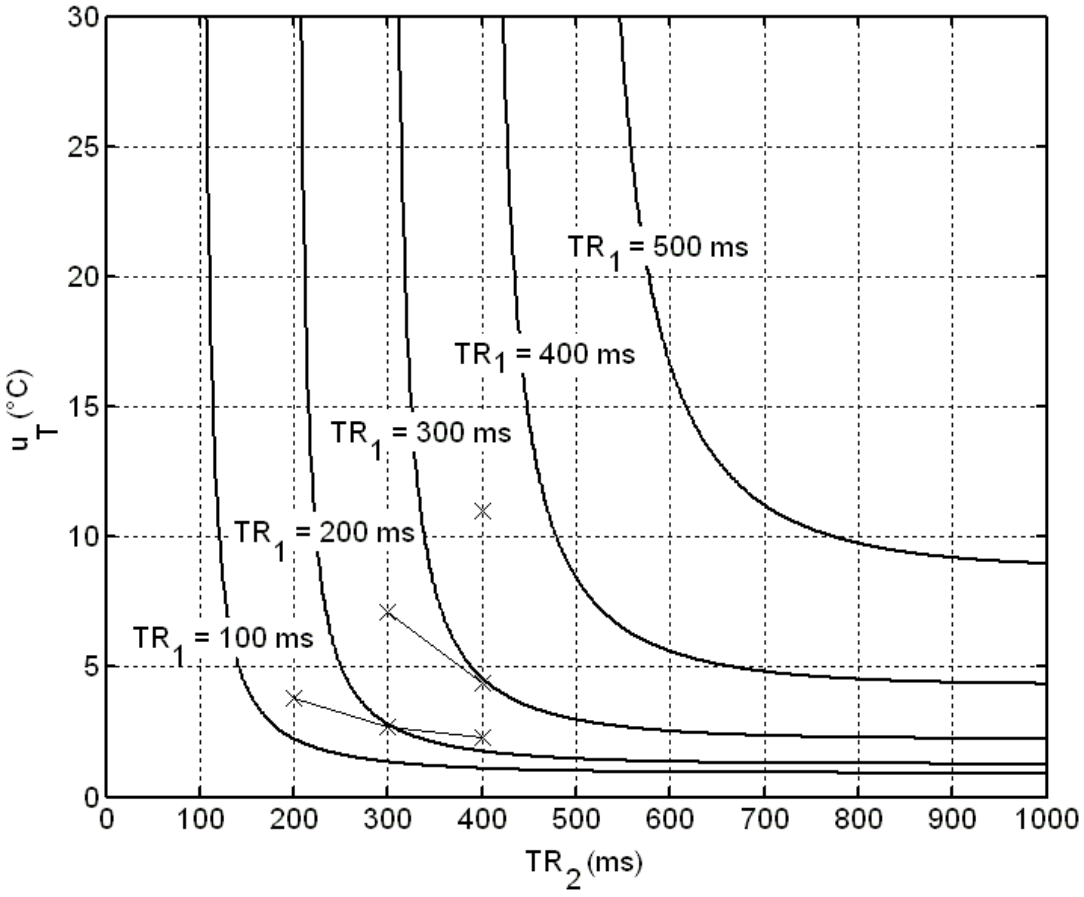
30
25
20
15
10
5
0
0
100
200
300
400
500
600
700
800
900
1000
u T (°C)
TR2 (ms)
TR1 = 500 ms
TR1 = 400 ms
TR1 = 300 ms
TR1 = 200 ms
TR1 = 100 ms

Figure3

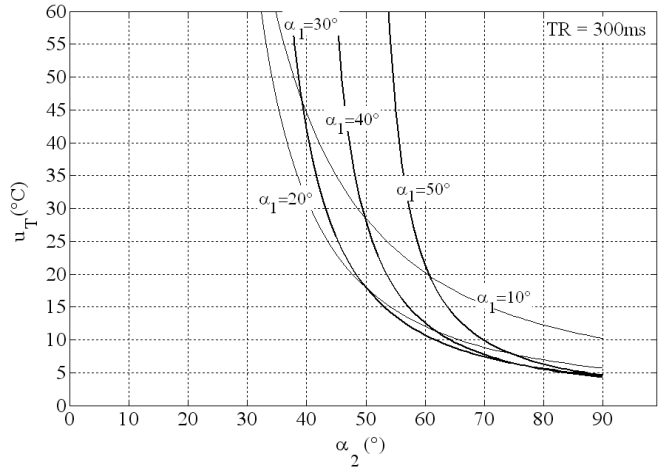
TR = 300ms
α1=30°
α1=40°
α1=20°
α1=50°
α1=10°
uT(°C)
α2 (°)

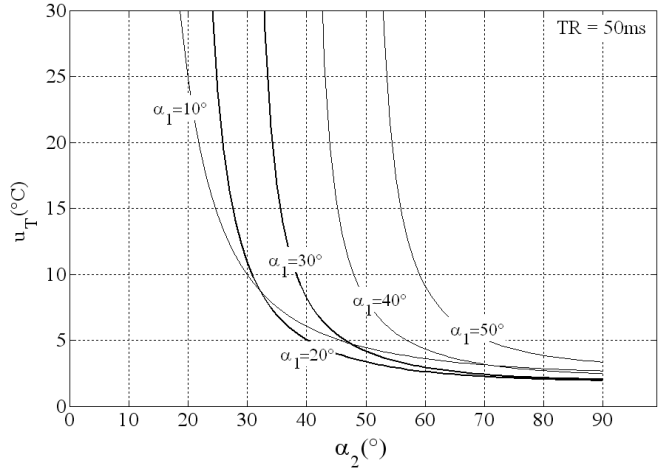
TR = 50ms
α1=10°
α1=30°
α1=40°
α1=50°
α1=20°
uT(°C)
α2(°)

Figure4

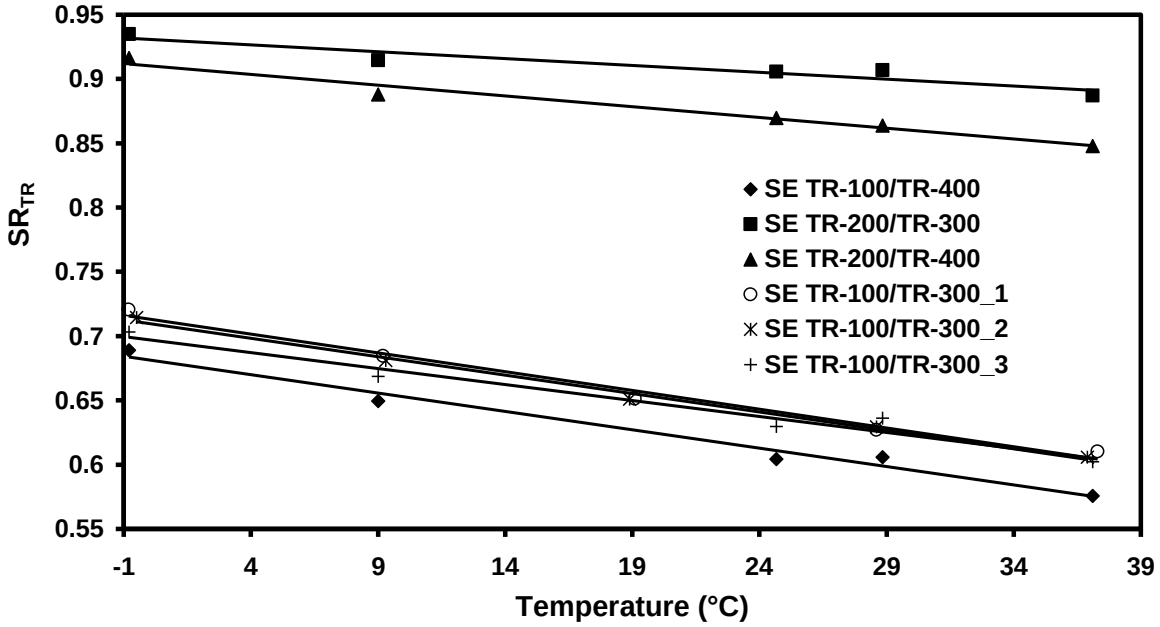
0.95
0.9
0.85
0.8
0.75
0.7
0.65
0.6
0.55
SR_TR
-1
4
9
14
19
24
29
34
39
Temperature (°C)
SE TR-100/TR-400
SE TR-200/TR-300
SE TR-200/TR-400
SE TR-100/TR-300_1
SE TR-100/TR-300_2
SE TR-100/TR-300_3

Figure5

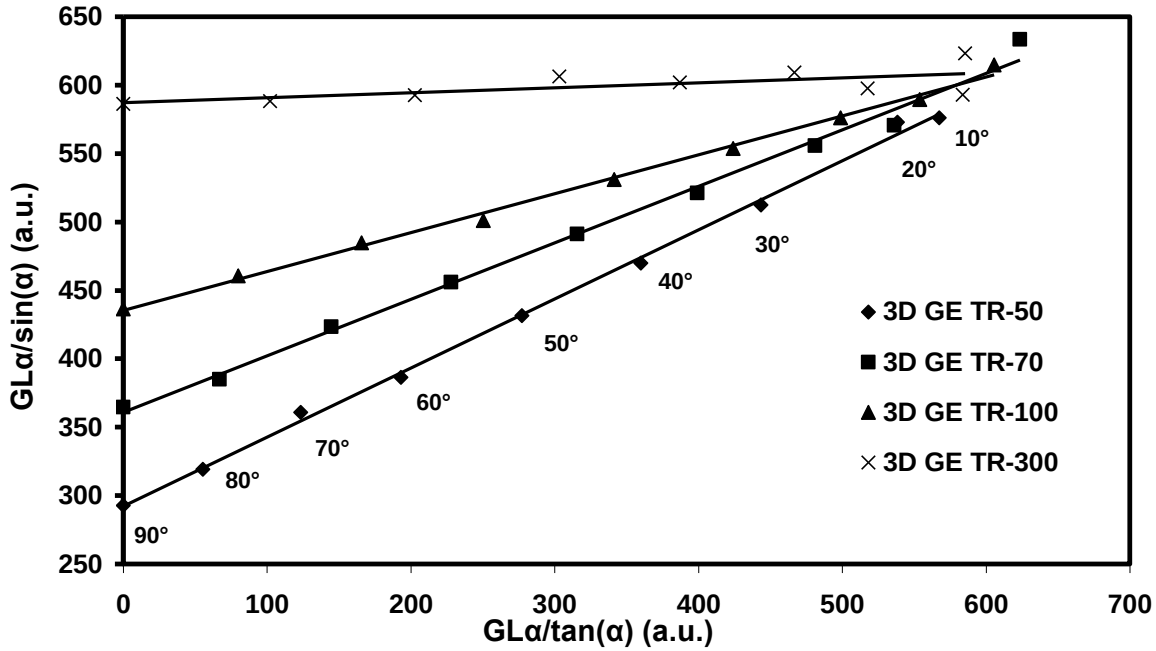
650
600
550
500
450
400
350
300
250
0
100
200
300
400
500
600
700
GLα/sin(α) (a.u.)
GLα/tan(α) (a.u.)
10°
20°
30°
40°
50°
60°
70°
80°
90°
3D GE TR-50
3D GE TR-70
3D GE TR-100
3D GE TR-300

Figure6

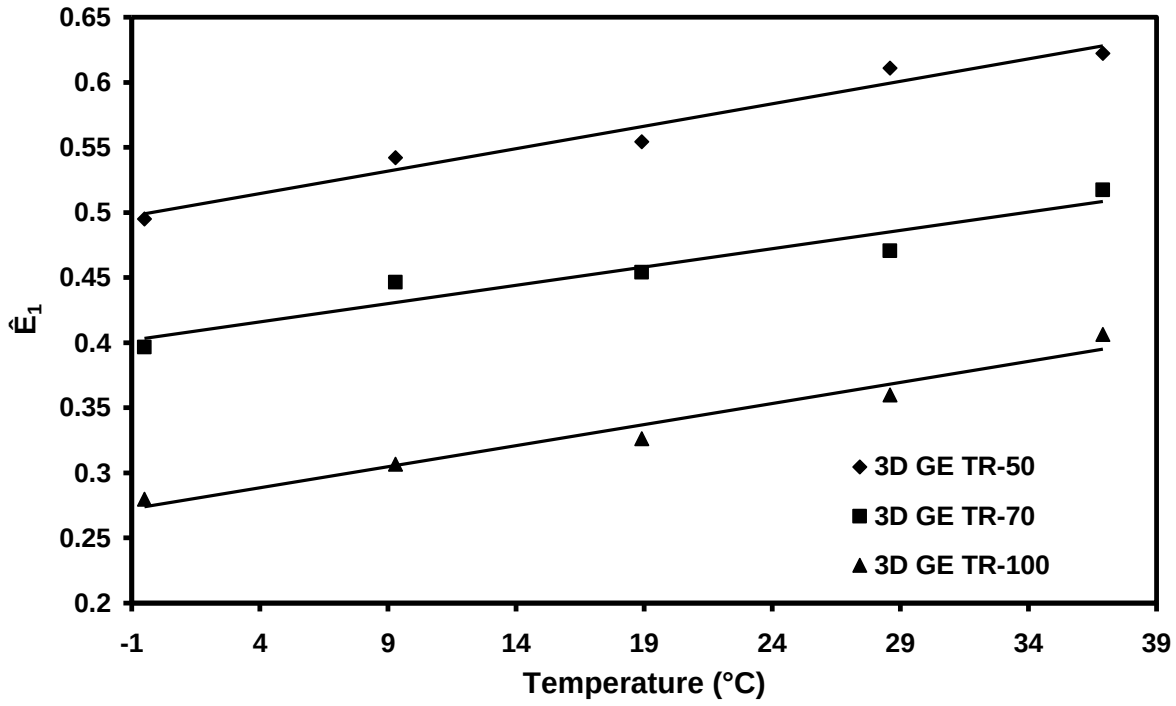
0.65
0.6
0.55
0.5
0.45
0.4
0.35
0.3
0.25
0.2
$\hat{E}_1$
-1
4
9
14
19
24
29
34
39
Temperature (°C)
3D GE TR-50
3D GE TR-70
3D GE TR-100

Figure7

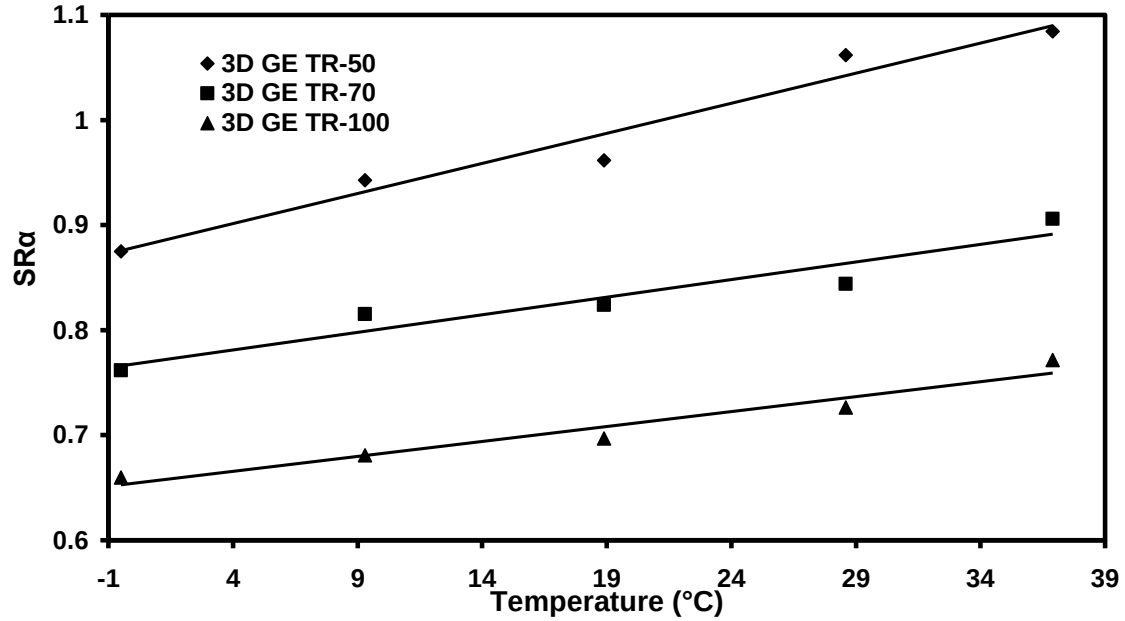
3D GE TR-50
3D GE TR-70
3D GE TR-100
SRα
1.1
1
0.9
0.8
0.7
0.6
-1
4
9
14
19
24
29
34
39
Temperature (°C)

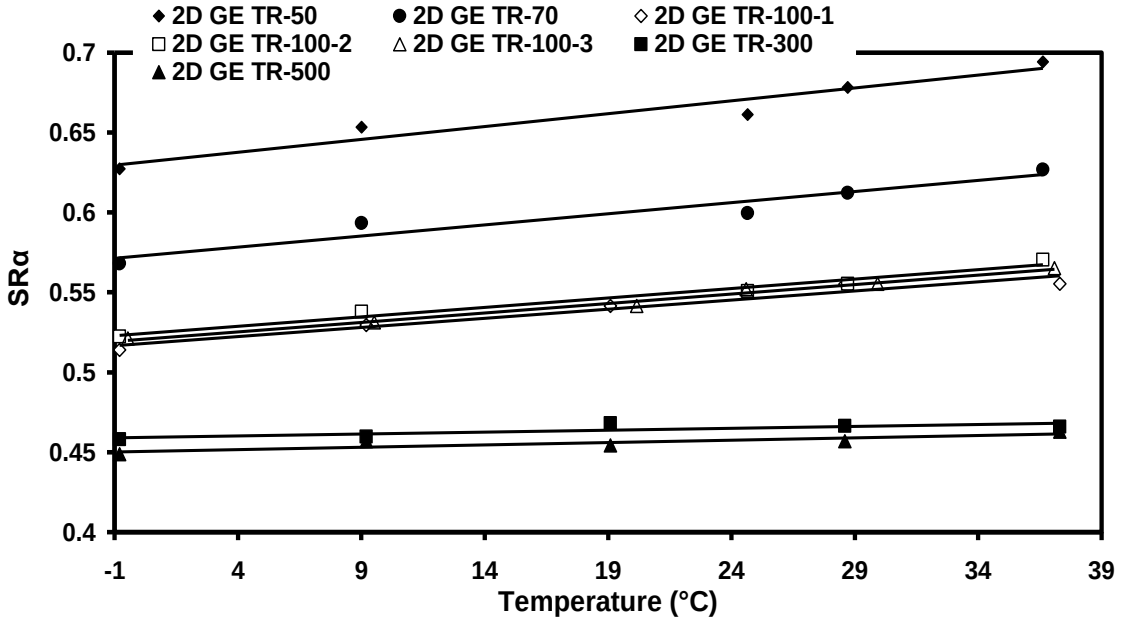
2D GE TR-50
2D GE TR-70
2D GE TR-100-1
2D GE TR-100-2
2D GE TR-100-3
2D GE TR-300
2D GE TR-500
SRα
0.7
0.65
0.6
0.55
0.5
0.45
0.4
-1
4
9
14
19
24
29
34
39
Temperature (°C)

Figure8

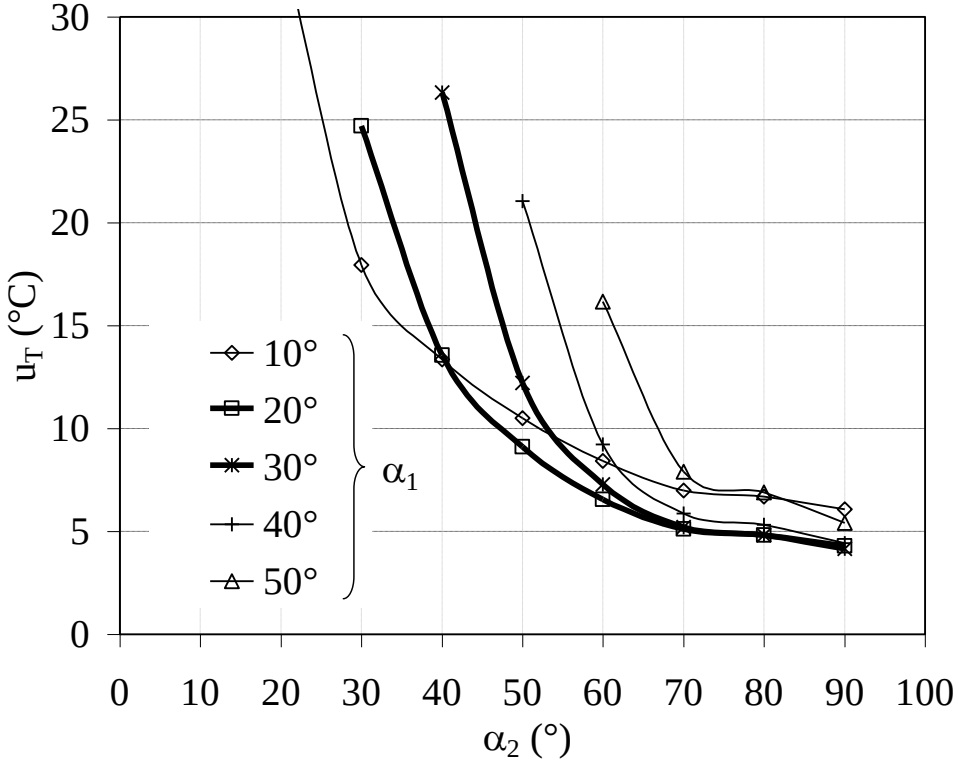
30
25
20
15
10
5
0
u_T (°C)
0
10
20
30
40
50
60
70
80
90
100
α_2 (°)
10°
20°
30°
40°
50°
α_1

Figure9

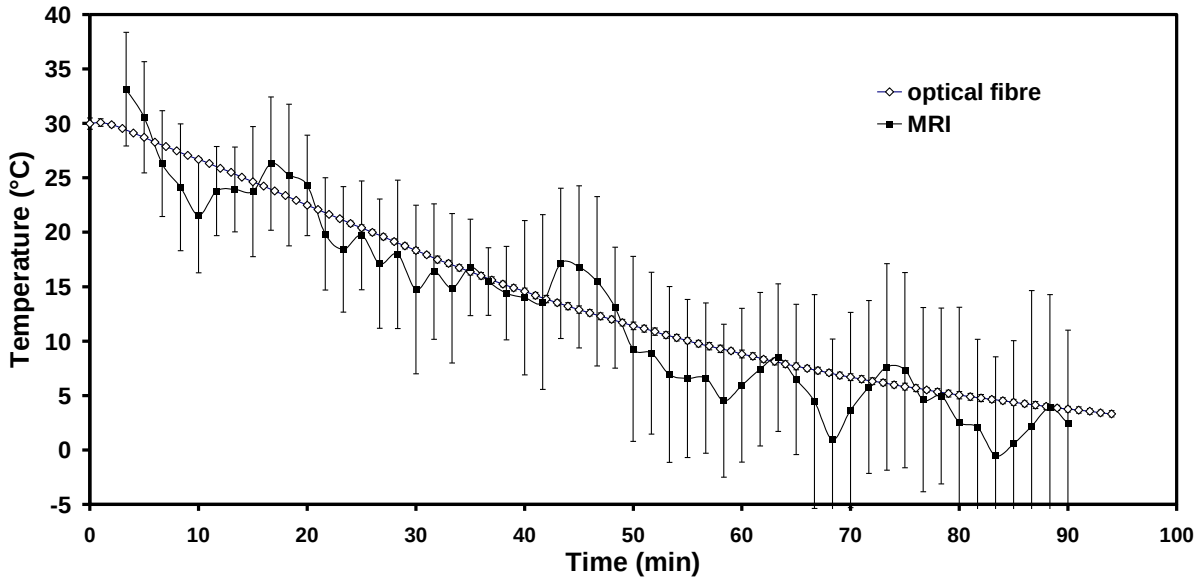
Temperature (°C)
Time (min)
optical fibre
MRI
40
35
30
25
20
15
10
5
0
-5
0
10
20
30
40
50
60
70
80
90
100

Figure10

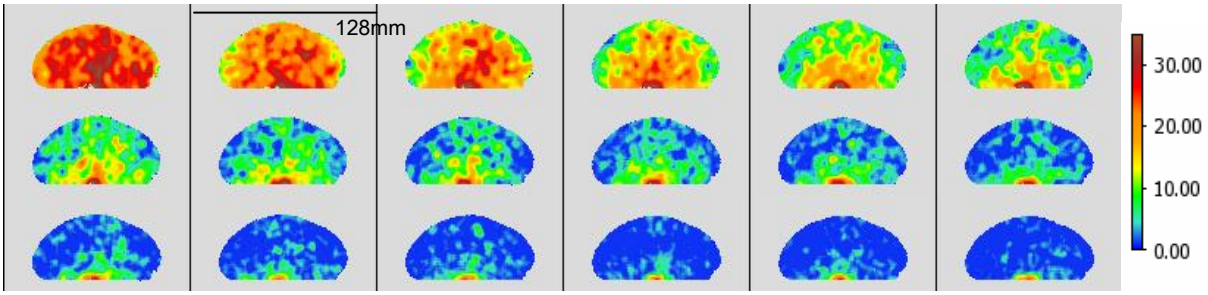

Table1

sequence	acquisition time	number of averages	repetition time (ms)	P	S/N ratio	uncertainties related to the model							uncertainties related to P			u_T
						a	u_a	b	u_b	$u_{a,b}$	R^2	C_{model}	u_P	u_P/P	C_P	
	(min-s)		(ms)			($10^{-3}.°C^{-1}$)	($10^{-3}.°C^{-1}$)	(a.u.)	(a.u.)	($10^{-7}.°C^{-1}$)		(%)		(%)	(%)	(°C)
SE sequence	3min17	4	100/300 (run1)	SR_{TR}	21	-2.9	0.2	0.713	0.005	-7.4	0.99	2	0.034	5	98	2.4
			100/300 (run2)		20	-2.9	0.1	0.710	0.003	-3.0	0.99	1	0.036	5	99	2.5
			100/300 (run3)		21	-2.5	0.3	0.697	0.007	-14.9	0.96	4	0.033	5	96	2.7
			100/300 (run4)		19	-2.6	0.1	0.678	0.002	-1.2	1.00	0	0.036	5	100	2.8
	1min40	2	100/300		16	-2.7	0.2	0.695	0.004	-4.8	0.99	1	0.044	6	99	3.3
	4min22	4	100/400		21	-2.9	0.2	0.682	0.006	-11.1	0.98	4	0.032	5	96	2.3
	4min22		200/300		25	-1.1	0.2	0.931	0.005	-8.6	0.90	2	0.037	4	98	7.1
	4min07		300/400		21	-0.7	0.1	0.978	0.003	-3.3	0.91	1	0.039	4	99	11.0
	2min37		100/200		25	-1.9	0.2	0.749	0.005	-7.3	0.97	2	0.036	5	98	3.8
	5min13		200/400		25	-1.7	0.2	0.910	0.004	-5.4	0.97	2	0.036	4	98	4.4
3D GE sequence	1min48	1	50	$\hat{E}_1$	7	3.4	0.4	0.501	0.009	-28.5	0.96	2	0.075	15	98	2.2
	2min30		70		5	2.8	0.5	0.405	0.011	-41.1	0.92	2	0.076	19	98	2.7
	3min32		100		3	3.2	0.4	0.275	0.008	-23.9	0.96	1	0.080	29	99	2.5
	1min48		50	SR_α	9	5.7	0.7	0.878	0.015	-81.3	0.96	2	0.100	11	98	1.8
	2min30		70		10	3.4	0.6	0.768	0.013	-64.6	0.92	3	0.076	10	97	2.3
	3min32		100		11	2.8	0.4	0.654	0.009	-28.6	0.95	2	0.060	9	98	2.1
2D GE sequence	1min42	8	50	SR_α	27	1.7	0.1	0.630	0.002	-2.2	0.99	1	0.023	4	99	2.7
	50s	4			19	1.9	0.1	0.631	0.002	-1.4	0.99	0	0.033	5	100	3.5
	1min46	6	70		24	1.5	0.1	0.571	0.002	-0.9	0.99	0	0.023	4	100	3.2
	1min10	4			20	1.5	0.1	0.569	0.001	-0.6	0.99	0	0.028	5	100	3.8
	1min42		100 (run1)		19	1.1	0.1	0.518	0.003	-4.0	0.95	2	0.026	5	98	4.7
			100 (run2)		21	1.2	0.1	0.524	0.003	-2.3	0.98	1	0.025	5	99	4.3
	1min42		100 (run3)		20	1.2	0.1	0.521	0.002	-0.9	0.99	0	0.026	5	100	4.3
	5min06		300		21	0.2	0.1	0.46	0.002	-1.9	0.64	2	0.022	5	98	18.7
	4min16	2	500		15	0.3	0.1	0.45	0.002	-1.7	0.76	1	0.030	7	98	20.8